ACS APPLIED MATERIALS & INTERFACES

Research Article

www.acsami.org

Direct Preparation of Few Layer Graphene Epoxy Nanocomposites from Untreated Flake Graphite

James Throckmorton and Giuseppe Palmese*

Department of Chemical and Biological Engineering, Drexel University, 3141 Chestnut Street, Philadelphia, Pennsylvania 19104, United States

ABSTRACT: The natural availability of flake graphite and the exceptional properties of graphene and graphene−polymer composites create a demand for simple, cost-effective, and scalable methods for top-down graphite exfoliation. This work presents a novel method of few layer graphite nanocomposite preparation directly from untreated flake graphite using a room temperature ionic liquid and laminar shear processing regimen. The ionic liquid serves both as a solvent and initiator for epoxy polymerization and is incorporated chemically into the matrix. This nanocomposite shows low electrical percolation (0.005 v/v) and low thickness (1−3 layers) graphite/graphene flakes by TEM. Additionally, the effect of processing conditions by rheometry and comparison with solvent-free conditions reveal the interactions between processing and matrix properties and provide insight into the theory of the chemical and physical exfoliation of graphite crystals and the resulting polymer matrix dispersion. An interaction model that correlates the interlayer shear physics of graphite flakes and processing parameters is proposed and tested.

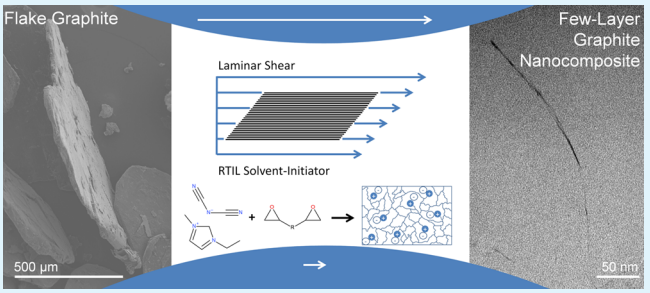

KEYWORDS: *laminar shear, exfoliation, few layer graphite, graphene, nanocomposite, ionic liquid*

INTRODUCTION

Once isolated, atomically thin graphene possesses exceptional native properties. For composite applications, tensile modulus, electrical conductivity, and thermal conductivity are of particular interest.[1] In addition to these intrinsic properties, graphene is an outstanding secondary phase for composite materials, providing a high specific surface area (2630 m^2/g), two-dimensional loadbearing capacity, high aspect ratio, and low-cost promise,[2,3] due to the ready availability of large amounts of graphene in the form of natural graphite (>800 m metric tons estimated worldwide).[4] Thus, the scalable, top-down exfoliation of graphite into its graphene layers without disrupting the native sp^2-hybridization remains a high priority research target. Taking into account an understanding of graphite crystal structure, shear forces, solvent selection, dispersion, and polymer cure, this work proposes that well-defined laminar shear can exfoliate natural graphite at high yield. The approach provides a path to streamlined and scalable processing; it also avoids limitations of other exfoliation methods.

A variety of physicochemical strategies for graphite exfoliation have shown trade-offs between purity of exfoliated material, throughput, yield, and scalability for the exfoliation of natural graphite.[5] These approaches include covalent modification, graphite intercalation, electrochemical exfoliation, and mechanically assisted direct solvent dispersion. Covalent modification for graphite[6] provides for customizable surface chemistry[7] at the expense of the pristine nature of the graphene sheet. The most common graphite functionalization for exfoliation or further reaction is the oxidation[8] of graphite. Graphite oxide shows an increased interlayer spacing (6−8 Å, vs 3.35 Å for pristine, AB-stacked graphite), a disruption of sp^2 hybridization, and hydroxyl and epoxide groups on the sheet surfaces with a C:O ratio between 1.3:1 and 2.3:1.[8] These defect sites allow for further modification for solvation or further covalent linkages, and can be partially reduced to regain some graphene properties. Reduced graphene oxide sheets demonstrate a partially restored sp^2 hybridization, a C:O ratio of 5:1 to 10:1,[8] the creation of 5- and 7-membered ring defects,[9] and partially restored electrical conductivity.

Another strategy for the partial exfoliation of graphite is the use of graphite intercalation compounds (GICs).[4] GICs interact electronically with the graphitic carbon, penetrating the interlayer galleries without covalently interacting with the graphite sheets. The excitation of GICs by heating or microwave irradiation produces a rapid expansion of the graphite to hundreds of times its original volume. These expanded graphite structures can be mechanically separated to produce nanoplatelets of uniform dimensions, with thicknesses as small as 20 layers.

Recently, direct liquid exfoliation methods have been proposed involving a suitable graphene solvent and an effective kinetic dispersion method. Experimental studies using physical exfoliation methods followed by centrifugation have yielded a

Received: April 23, 2015
Accepted: June 15, 2015
Published: June 15, 2015

DOI: 10.1021/acsami.5b03465
ACS Appl. Mater. Interfaces 2015, 7, 14870−14877

library of effective solvents.[10−12] Additionally, theoretical studies have identified specific interactions between graphene and a variety of solvent molecules,[13] with $\pi-\pi$ stacking and ionic charge sharing as primary mechanisms for effective graphene solvation. Moreover, a variety of solvent interaction potentials have been proposed and experimentally verified.[10]

Of particular interest for this study, imidazolium-based room-temperature ionic liquids (RTILs) form a class of compounds[14] with tunable[15] reaction and solvent chemistries that offer unique opportunities for graphite exfoliation and dispersion. Previous research has shown direct exfoliation and dispersion of graphene in such solvents electrochemically.[16−18] Theoretical studies have shown that imidazolium-based RTILs interact with graphene, carbon nanotubes, and other sp^2-hybrided carbon structures through cation$-\pi$ stacking,[19] interlayer intercalation, and electrostatic shielding.[20] Our work has also shown that some imidazolium RTILs also initiate the polymerization of epoxies[21] and can therefore serve both as solvents and curing agent eliminating the problematic and costly need to remove solvents during processing.[22−24]

Although an optimized chemistry provides for a thermodynamically stable or metastable suspension, kinetic forces are required to overcome interlayer attraction and achieve exfoliation. Sonication is the most common kinetic treatment presented in the literature, but potential applications are limited by treatment time, cleavage, and oxidation. Ultrasonication provides a variety of physical forces via frequency-modulated compression/rarefication waves, featuring turbulent fluid flow and violent cavitation events.[25] To the nanoparticle, these processes result in extreme local conditions including pressure up to 1000 bar, temperature up to 5000 K, liquid velocity reaching 280 m/s, and cooling rate above 10 K/s.[26] Sonication acts to peel the peripheral layers from the graphitic stack, and requires significant treatment time to act on interior layers.[27] Further, sonication has a marked effect on particle size, cutting sheet size in addition to interlayer exfoliation.[28] Finally, evidence also exists of altered surface chemistry for sonicated particles.[29,18]

A variety of methods for applying direct mechanical shear, including grinding,[30] twin-screw extrusion,[31] high-shear ball-milling,[32,33] rotor-stator mixing,[34] and impeller-driven mixing[35] have shown the ability to exfoliate graphite directly in an appropriate solvent. Of special significance to this study, laminar shear from a 3-roll mill is a physical approach that has been successfully used for nanoparticle dispersion and nanocomposite preparation. Researchers have applied high-shear milling separately to the exfoliation of graphite[36] and the dispersion of nanoclays,[37] acid-expanded graphite nanoplatelets,[22,38,39] and carbon nanotubes[23,24,40−42] for nanocomposites.

This work presents an alternative to chemical processing and chaotic flow-fields for the direct exfoliation of graphite and the single-pot preparaton of nanocomposites. In this approach, exfoliation is accomplished by combining the application of a high-shear laminar flow pattern using a 3-roll mill, and the use of an RTIL solvent/initiator to minimize reaglomeration and induce composite cure. Additionally, we develop a theoretical approach to predict degree of exfoliation by combining the physical understanding of laminar flow through a 3-roll mill the latest understanding of graphite interlayer shear strength values. When this understanding is combined with the RTIL solvent-initiator processing previously demonstrated by our lab,[21−24] a simple, integrated procedure for graphite exfoliation, graphene dispersion, and polymer cure is presented here.

RESULTS AND DISCUSSION

Design of Experiment. Two critical factors are considered for direct graphite nanocomposite preparation from flake graphite: applied shear stress and dispersion chemistry. Shear stress is required for exfoliation, whereas a good solvent environment prevents restacking. With these considerations in mind, flake graphite (nominal thickness 20−50 μm) is mixed into a solution of Epon 828 and 1-ethyl-3-methyl imidazolium dicyanamide (EMIM-DCN). This suspension is then processed with a 3-roll mill, and thermally cured. As a control, the same processing schedule is performed on a suspension of graphite directly in Epon 828 with no solvent. Subsequent to processing, this control suspension is mixed with and cured by Primaset LECY curing agent.

For 3-roll mill processing, the maximum shear is encountered in the regions between adjacent rollers, known as the nips. The nip width can be adjusted to balance the need for throughput of thick flakes (which require wide nips) and high applied shear stresses (which require narrow nips). Thus, a variable nip-width processing schedule, detailed in Table 1, was developed. In this experiment, a suspension of flake graphite passes through the 3-roll mill 30 times with successively narrowing nip widths and correspondingly increasing shear. The application of shear at the wide nips begins the process of exfoliation on large flakes, with shear sliding occurring between their weakest planes. As the nips narrow, thinner flakes with stronger interlayer association are exposed to sufficient shear stress for complete exfoliation.

Table 1. 30-pass Variable Roll-Nip Procedure Showing the Decrease in Nip Width, Corresponding to an Increase in Applied Shear Stress

run number	nip width (μm)
1	550
2	300
3−10	50
11−20	20
21−30	5

Samples are removed at various stages of this processing scheme for analysis and cure. While still in the liquid state, solution rheology measures degree of exfoliation. For cured samples, electrical conductivity measures the dispersion of the percolating nanofiller network. Additionally, X-ray diffraction (XRD) on the cured composite provides information on deviation from graphite crystal structure, indicating exfoliation effectiveness. Qualitatively, microscopy provides information about the structure of the cured material, the exfoliated size of the nanofiller material, and the effect of processing on exfoliation and dispersion.

RTIL-Shear Processing. Figure 1 shows the viscosity of the liquid 3 wt % graphite/RTIL/epoxy suspension before, during, and after processing. Significantly, minimal viscosity increase occurs upon the addition of unexfoliated graphite flakes. Instead, two significant increases in solution viscosity are noted. The first is between unprocessed graphite solution and the graphite solution that has been processed 5 times, through 550, 300, and 50 μm nip widths. This small viscosity increase continues through additional 50 μm processing and 20 μm processing. The next large increase in viscosity occurs when the shear was increased at the smallest nip width (5 μm). Here, in addition to the increase in viscosity, a strong shear-thinning

DOI: 10.1021/acsami.5b03465
ACS Appl. Mater. Interfaces 2015, 7, 14870−14877

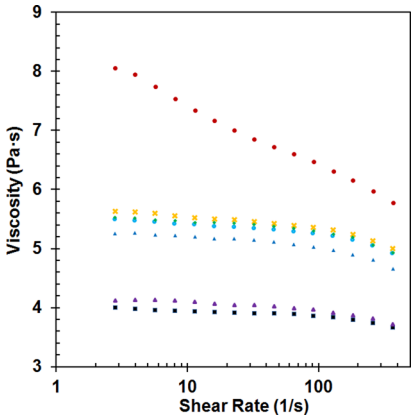

Figure 1. Rheometry of graphite/epoxy/RTIL slurry during processing. As graphite is exfoliated by shear processing, the solution viscosity increases as well as showing the shear-thinning behavior characteristic of high aspect ratio suspended particles. 15% RTIL/85% EPON 828 solution without graphite (■), graphite/RTIL/epoxy with no processing (purple ▲), and the graphite suspension after varying degrees of 3-roll mill processing – 5 passes through the mill, 50 μm minimum nip width (blue ▲), 10 passes/50 μm nip (○), 15 passes/20 μm nip (♦), 20 passes/20 μm nip (×), and 30 passes/5 μm nip (●).

effect is noted. This is consistent with the behavior of colloidal suspensions of high aspect ratio particles as a result of the alignment of flakes within the stronger flow field.[43] This shear thinning can be taken as a second indicator of the increased aspect ratio of suspended particles, along with the viscosity increase itself.

X-ray diffraction peaks of cured composite samples are shown in Figure 2. The 002 peak of graphite (appearing here at

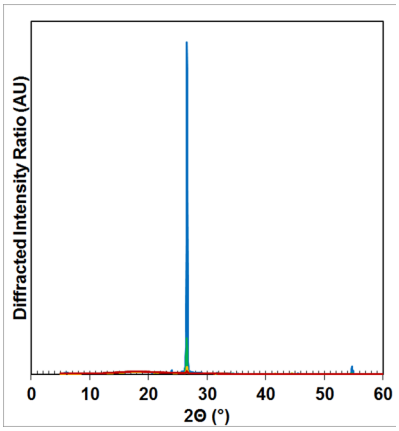

Figure 2. X-ray diffraction of the cured composites of 3% graphite processed through various degrees of 3-roll mill processing – 2 passes/250μm nip (purple —), 10 passes/50 μm nip (green —), 20 passes/20 μm nip (yellow —), and 30 passes/5 μm nip (red —).

$2\theta = 26.56°$), which corresponds to interlayer stacking between layers in the graphite crystal, disappears quickly with processing. The 2-pass composite was chosen for the baseline rather than the untreated sample to attempt to avoid the effects of sedimentation on the measurement. The composite made from material processed with the full 30-pass procedure had a 002 peak of less than 1% of the value of the composite made after 2 passes of 3-roll processing. This is an indication of an interruption of the native graphite interlayer stacking.

Electrical conductivity is both a desirable property for a nanocomposite material and an excellent indicator of internal structure through the measurement of bulk properties. Figure 3

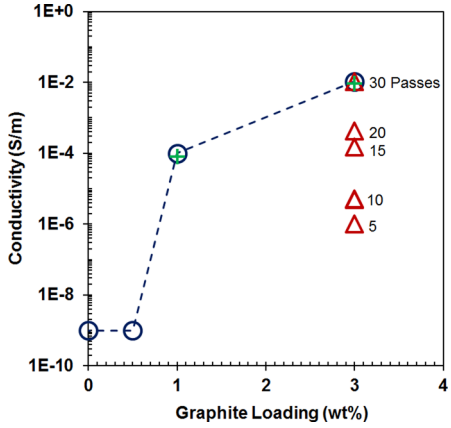

Figure 3. Conductivity versus processing and loading. 0, 0.5, 1, and 3 wt % graphite processed via a full 30-pass variable gap methodology with conductivity measured horizontally (○) and vertically (+) with respect to cure. For 3 wt % graphite, in addition to the final product, samples were removed at select processing steps (numbers indicated on the chart), cured, and measured for electrical conductivity (Δ).

shows the DC electrical conductivity of graphite, showing the effect of graphite loading, the anisotropy of the cured material, and the effect of processing for the 3 wt % loading. DC conductivity increased monotonically with processing, and showed the greatest improvements after the decreases in layer thicknesses after the nip width reduction at 10 and 20 passes, confirming the effect of shear stress on exfoliation and dispersion state. The large increase in electrical conductivity between 0.5 and 1 wt % (0.26 and 0.51 vol %) indicates the formation of a percolating network of the conductive graphite phase within the insulative matrix. This is lower than the percolation threshold of graphite nanoplatelet composites (between 0.5 and 1 vol %, depending on aspect ratio),[22] and indicates true nanoscale dispersion of graphene flakes.

For conductive particles with flake geometry, percolation threshold has been shown to vary with aspect ratio:[44]

$$f_c = \frac{27}{4\alpha} \quad (1)$$

(where f_c is the percolation threshold in volume fraction, and α is the aspect ratio). Using this equation and the measured percolation threshold, an effective aspect ratio for dispersed graphite processed by this method can be found to be at least 1300, significantly higher than the initial aspect ratio of ~20 (given nominal 30 × 600 μm flakes).

Additionally, electrical conductivity anisotropy was considered. In an unstable suspension, sedimentation causes conductivity horizontal with respect to curing dimensions to be significantly higher than vertical conductivity. Gel time under the polymer cure conditions presented in this work is 8 h, giving time for sedimentation to occur if the suspension is unstable. After full processing, the samples in this study showed minimal anisotropy, well within the margin of measurement error.

Figure 4 shows electron microscopy images before, during and after processing, providing insight into the exfoliation status, microstructure, and size of the particles after full

DOI: 10.1021/acsami.5b03465
ACS Appl. Mater. Interfaces 2015, 7, 14870–14877

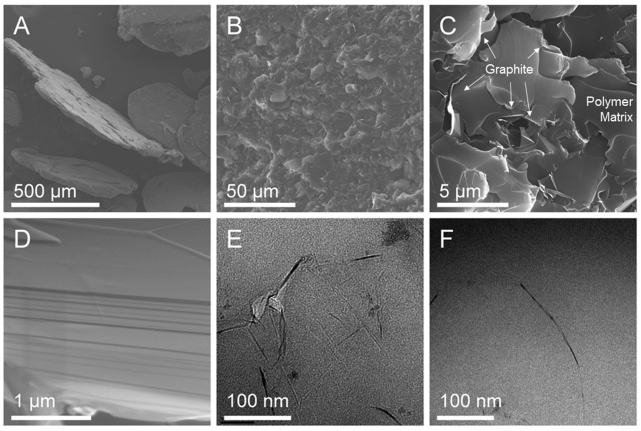

Figure 4. Microscopic images of unmodified graphite flakes (A) and fracture surfaces of cured graphite composites (B–F). (A) Unmodified graphite flakes +100 mesh graphite flakes. (B,C) Fracture surfaces of 3% graphite processed with the full 30 pass processing at two length scales. These show graphite uniformly distributed throughout the composite, at significant reductions in both layer thickness and diameter. (D) Graphite stack on the fracture surface of a 3% graphite composite after 20 passes in the 3 roll mill shows a slipped-layer morphology. (E,F) TEM images of 1% graphite at 30 passes shows both folded graphene sheets (E) when the microtome cut is parallel to the sheet, and thicknesses reaching less than 1 nm (1–3 graphite layers) when the microtome is perpendicular to the graphene sheet (F).

processing. Figure 4A shows a picture of the +100 mesh graphite flakes without treatment. The starting material has diameters in the range of 300–700 μm, and thicknesses from 20 to 50 μm, corresponding to 60 000–150 000 individual graphene layers. Figure 4B,C shows the fracture surface of a 3% graphite composite material after 30 3-roll mill passes, with thin, well-dispersed graphite/graphene plates throughout the bulk of the polymer. Figure 4D (3% graphite, 20 mill passes/20 μm nip width) shows a partially sheared graphite stack reveals weaker/stronger layers as parts of the stack remain unsheared, whereas other layers have experienced significant shearing. Finally, Figure 4E,F shows TEM images of 1% graphite composites after the full 30-pass milling schedule. Figure 4E shows a bent face sheet of graphene/few layer graphite on the surface of the microtomed region. The pleating and folding of the sheet reveals a morphology typically shown by graphene, rather than bulk graphite, the parallel structure of which resists bending to high angles. Figure 4F shows a side view of a graphite sheet in the cured epoxy, with a measured width of 1.0 nm, consisting of 1–3 layers. These TEM images indicate that the distribution of graphite widths within the cured composite includes very few layer graphite or graphene.

Figure 5 shows the mechanical results of graphite nanocomposites treated with 30 passes through the 3-roll mill. As with many graphene nanocomposites, an increase in modulus is found, along with a decrease in ultimate tensile strength. The modulus increase due to the stiffer carbon stage is similar to other graphite composites.[22] The drop in strength is also commonly reported in large aspect ratio plate composites as a result of low interfacial strength along the graphitic surface.[45]

Solvent-free Processing. For comparison with the RTIL-shear dispersed process, 3% graphite was milled directly in EPON 828 with no solvent. The same 30-pass procedure, at the same nip widths as the RTIL-shear processing method was performed. The solvent-free dispersion had higher viscosity,

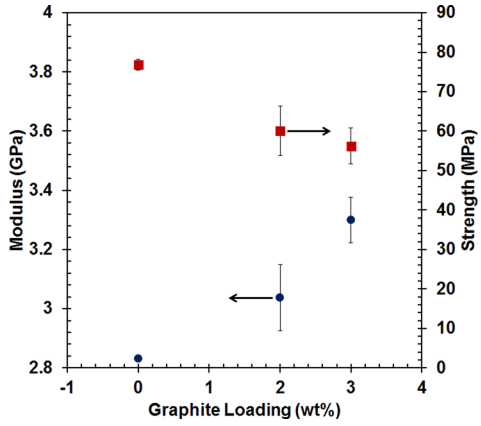

Figure 5. Mechanical performance of graphite nanocomposite manufactured using the variable-gap size model and RTIL solvent. With increased loading, an increase in tensile modulus and a decrease in tensile strength are observed.

and thus higher shear forces, than the RTIL-dispersed graphite solution. Figure 6 shows the viscosity increase for both the

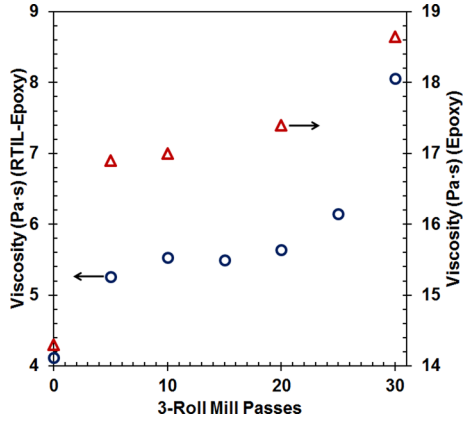

Figure 6. Viscosity increase at 25 °C and a shear rate of 2 s^{-1} versus processing for 3% RTIL-dispersed graphite (○) and 3% solvent free (EPON 828) dispersed graphite (Δ).

RTIL-dispersion and the solvent free dispersion. Both showed similar trends in viscosity increase, with the largest jumps in viscosity happening upon initial processing and at the low roller nip width. Further, for solvent-free processing, the viscosity increase is higher at early processing steps, as a reflection of the higher shear forces present due to the higher viscosity of the solvent-free suspension.

Figure 7 shows the decrease in XRD peak heights of cured epoxy composites made with solvent-free and RTIL-dispersed graphite. As a baseline, composite made after 2-pass 3-roll mill processing were used to minimize sedimentation and mixing effects. Both series show an exponential decrease in the graphite 002 peak height (normalized with the amorphous polymer peak at 2θ = 18.2°). The solvent-free dispersion initially shows greater exfoliation, but the results are similar after the full processing range at narrow gap size. This data shows only the effect of the shear processing, not dispersion. Once exfoliated, graphite can either be dispersed throughout the composite material or restack in amorphous agglomerates.

Despite the exfoliation indicated in rheometric and XRD studies, poor dispersion was indicated by the lack of property improvement of the solvent-free system. All solvent free

DOI: 10.1021/acsami.5b03465
ACS Appl. Mater. Interfaces 2015, 7, 14870–14877

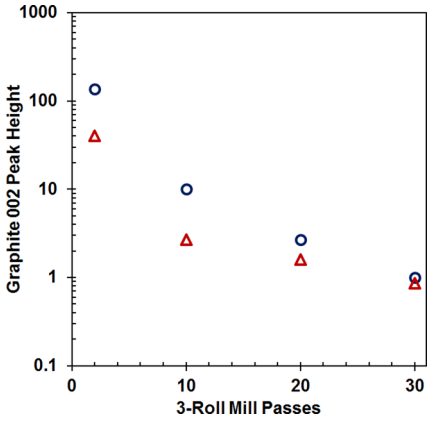

Figure 7. XRD peak height ratios (graphite 002/amorphous polymer peak) for 3% RTIL-dispersed graphite (○) and 3% solvent free (EPON 828) dispersed graphite (Δ) in the cured composite for 2, 10, 20, and 30 3-roll mill passes. This shows the exfoliation behavior of the graphite crystal in the composite material. For both situations, the graphite peak decreases exponentially with processing, indicating the exfoliation of graphite from its native crystal structure.

samples were tested for DC electrical conductivity with an experimental setup with sensitivity to conductances as low as 10^{-7} S/m (a level at which RTIL-dispersed graphite composites showed significant conductivity after 5 passes, Figure 3). No solvent-free sample surpassed this threshold of electrical conductivity, indicating that whatever the exfoliation state (indicated by rheometry and XRD), the dispersion state was ineffective at forming a percolating network of the conductive graphite phase.

Finally, a comparison of the visual dispersion of RTIL-dispersed and solvent-free graphite composites in Figure 8

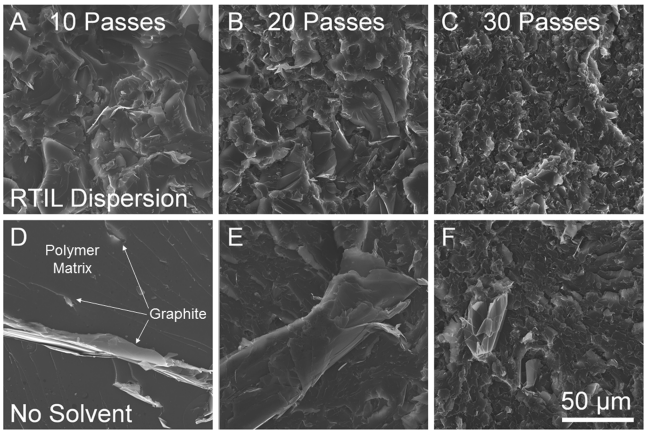

Figure 8. Dispersion SEMs of RTIL-dispersed graphite flakes (A–C) and solvent-free dispersed graphite flakes (D–F), at 10 (A,D), 20 (B,E), and 30 (C,F) passes through the 3-roll mill. At each stage, the RTIL-dispersed graphene flakes show more uniform dispersion throughout the material, despite the similarity of forces.

reveals differences in bulk dispersion. For the RTIL-dispersed composite, further processing at higher shear decreases the diameter of graphite particles (Figure 8A–C). Additionally, because of the improved electrical conductivity (which goes as a function of aspect ratio), we can also conclude that the decrease in thickness occurs even faster than the decrease in particle diameter. Significantly, even as this process occurs, the partially exfoliated graphite is always well dispersed throughout the bulk of the material.

This is not the case for the solvent-free dispersion (Figure 8D–F). Here, a reduction in diameter and thickness is also directly observed. However, SEM reveals two significant distinctions in the dispersion of graphite in the solvent-free composite, relative to the RTIL-dispersed composite. First, significant areas of material with no graphite exist in the composite. Second, large, randomly associated graphite stacks are noted at each length scale. This indicates graphite that partially restacked to other graphite rather than exist in the solvent environment of the bulk material.

On the basis of the SEM, rheometry, and XRD results, this restacking is not a full restoration of native graphite with pristine crystal structure. Rather than perfect sheet alignment, exfoliated graphite flakes partially align and form amorphous structures. This restacking reduces the effective aspect ratio of the agglomerate, preventing the formation of a percolating network, even at concentrations well above the percolation threshold for similarly processed, but well-dispersed graphite sheets. Taken together, the rheometric, electrical, and microscopic comparison between the RTIL-shear dispersion and the solvent free-shear dispersion reveal that although shear stresses alone induces exfoliation in graphite sheets, a good solvent environment is necessary for effective dispersion within a liquid solution or a bulk composite.

Theory. To consider the effect of processing on a graphite crystal, an integrated model is developed that incorporates the physical parameters of a 3-roll mill, the fluid dynamics of the suspension, and the internal resistance to shear of the graphite flake. Figure 9 shows the path of the graphite suspension

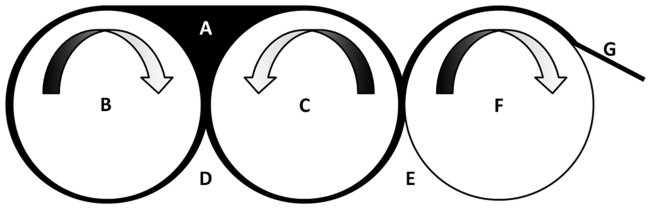

Figure 9. 2-D schematic of a 3-roll mill. The sample is injected into the feed region (A) between the feed roll (B) and the center roll (C). Initially, the bulk of the material remains in the feed region while small amounts pass through the first high-shear nip (D) and remain adhered to the rollers as they are alternatively recirculated into the feed region by the feed roll or advanced to the second nip (E) by the center roll. After passing through the second nip, the material is again either recirculated into the feed region by the center roll, or adheres to the apron roll (F) and is removed by the apron (G) for collection and further characterization.

through the 3 rolls of the mill. The three rollers (Figure 9B,C,F) rotate at increasing speeds: 31, 84, and 174 rpm (corresponding to surface velocities of 0.1, 0.27, and 0.57 m/s). The velocity differential between consecutive rollers produces high-shear environments between the rollers at their points of closest approach. Starting in the feed region (Figure 9A), the sample moves through these two high-shear nips (Figure 9 D,E), and either recirculates back to the feed region or is deposited on the apron (Figure 9G).

Assuming static, isobaric, laminar flow between parallel plates, the fluid shear stresses (τ) of this 3-roll mill can be approximated as a function of viscosity (μ), roller surface

DOI: 10.1021/acsami.5b03465
ACS Appl. Mater. Interfaces 2015, 7, 14870–14877

velocities (u_1 and u_2), and nip width (L) using the standard equation for shear stress under Couette flow:

$$\tau = \frac{\mu(u_2 - u_1)}{L} \quad (2)$$

This approximated shear stress can then be compared with literature values of graphite interlayer shear stresses (ISS). Literature proposes a wide range of graphite ISS values, from 0.25[46] to 140 MPa.[47] This variability is due to deviations from ideal, AB-stacked graphite crystal structure. Classical studies did not account for variations in layer interactions, and thus reported a low value for graphite ISS by shearing a graphite crystal between the layers with weakest association.[46] Recent theoretical studies have shown substantial variations in sliding energies due to the thickness and number of graphene layers,[48] orientation of sliding layers,[49] layer stacking,[50] and shearing orientation. Moving from pristine crystals to real flakes, the presence of impurities and grain boundaries will add additional variables that affect the shear properties of a real graphite crystal.

Liu et al.[47] provide strong experimental evidence that interlayer stacking rotation is the key factor for variations within a single crystal, finding a 4 orders of magnitude change (0.5−140 MPa) in ISS from the same crystals before and after rotational perturbation. In this case, a lower value represents the shear required to induce sliding between randomly oriented layers (and corresponds to the numbers reported in earlier studies), whereas a higher number is required to induce sliding motion between pristine, AB-stacked layers. On the basis of this, it can be predicted that shear stresses above 0.5 MPa will shear a graphite crystal along randomly aligned layers, whereas stresses above 140 MPa will be required to induce shear exfoliation in pristine, AB-stacked layers.

Equation 2 predicts that the shear stress will be determined by the relative roller velocities, suspension viscosity, and nip width. On the experimental setup used for this experiment, roller velocities are fixed. Viscosity will increase over the length of the experiment as exfoliated graphite thickens the suspension. Thus, nip width is the primary experimental control over the shear experienced by a graphite flake within the mill.

Figure 10 plots shear against nip width for the viscosities (4.2, 5.3, and 8.2 Pa·s) corresponding to solutions with increasingly exfoliated graphite particles. Also depicted in Figure 10 are the ISS values for randomly- and AB-stacked graphite (horizontal dashed lines) and the nip widths used for processing (vertical dashed lines). This approximate model makes two predictions. First, shearing of randomly stacked-layers will occur for any nip width for this experiment, because all shear stresses are above 0.5 MPa. Finally, below 10−20 μm, the liquid shear stress exceeds the ISS of AB-stacked graphite for all experimentally relevant viscosities.

The predictions of this model reflect the experimental results well. The viscosity increases (Figures 1 and 6) occur primarily after initial shear processing, and after the nip width is set to 5 μm. This dual exfoliation behavior supports graphite ISS models that predict graphite to have tightly associated AB oriented interlayers and more loosely associated interlayers with a random rotational stacking. Additionally, electrical conductivity results (Figure 3) show the largest increases in conductivity after the gap thickness is narrowed at each processing step.

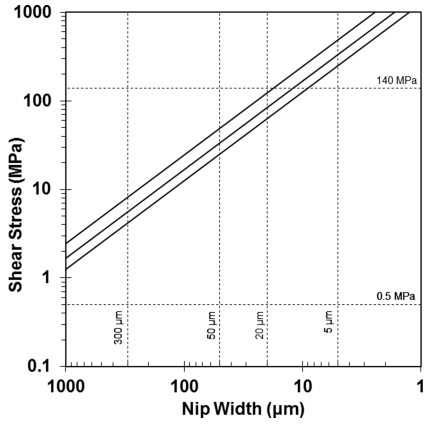

Figure 10. Applied stress seen by the surface of a suspended flake for for μ = 4.2, 5.3, and 8.2 Pa·s and the geometric considerations of the mill used in this study for a range of platelet thicknesses. Applied stress increases as the nip narrows. With a small enough nip, AB-stacked graphite layers can be successfully separated.

CONCLUSIONS

The primary conclusion to this study is that by a combination of mechanical shear and solvent selection, it is possible to make excellent graphene/few layer graphite nanocomposites without chemical treatment. Further, nanocomposite created by this method showed high electrical conductivity ($\sigma = 10^{-2}$ S/m at 3 wt %) a low electrical percolation threshold (φ_c = 1 wt %/0.5 vol %), and excellent qualitative graphite dispersion by SEM.

A second conclusion to this study is that the mechanism of exfoliation can be clearly understood from the anisotropic physics of graphite crystals with differing interlayer interactions. Significantly, a relationship between nanocomposite processing and graphite crystal properties can be shown. Further processing and application of higher shear forces increases both the liquid suspension viscosity and the electrical conductivity of the cured nanocomposite. This relationship between processing and exfoliation also confirms previous work on the shearing modes of a graphite crystal. The finding of significant increases in viscosity as processing shear reaches above the ISS of randomly oriented and AB-stacked graphene interlayers supports fundamental findings on the dual shearing modes of the graphite crystal.

Finally, this study shows that both effective application of shear forces and a good solvent are required for effective nanocomposite preparation. High shear forces were able to dramatically decrease the thickness of the original bulk graphite regardless of solvent presence. However, without a good solvent, composite material properties and microscopy revealed the spatial dispersion to be lacking and restacking to be a significant event.

MATERIALS AND METHODS

EMIM-DCN (EMD Sciences # 4.90163), DGEBA (Miller-Stephenson EPON 828, EEW 188 g/equiv), +100 mesh Flake Graphite (Sigma-Aldrich # 332461), (and 4,4-diaminodicyclohexylmethane (PACM curing agent, AirProducts, CAS # 1761-71-3) were used as received.

Samples were prepared by a modified form of the procedure previously presented by our group.[22] Flake graphite (0.01−.03 w/w) was mixed into a solution of ionic liquid and epoxy (17.6 phr EMIM-DCN relative to EPON 828). The solution was passed through the 3-roll mill 30 times through a variety of gap spacings, before the composite slurry was degassed and thermally cured at 80 °C for 12 h/120 °C for 2 h. Reference samples with PACM curing agent were

DOI: 10.1021/acsami.5b03465
ACS Appl. Mater. Interfaces 2015, 7, 14870−14877

processed with epoxy only, mixed with PACM, and cured at 80 °C for 4 h/160 °C for 2 h.

This mixture was milled in a 3-roll mill (Torrey Hills 2.5″ × 5″) with a 2.5″ roller diameter with roll speeds of 31, 84, and 174 rpm, corresponding to surface velocities of 0.1, 0.27, and 0.57 m/s. Shear was controlled by adjusting the thickness between rollers and the viscosity of the liquid solution. For all experiments, the gap size listed denotes the gap of both rollers. For larger roller thicknesses, the gap between the middle and apron roller are narrowed further at the end of a single run, to facilitate the full removal of material from the mill. Roller nip width was controlled by moving the rollers together onto a spacer of specified thickness. All thicknesses were verified by light microscopy, and the numbers presented for nip width are microscope measurements, not spacer thicknesses, which underreported the actual gap. For the smallest gap size (5 μm), a light was placed under the rolls and the rolls were adjusted to the minimum gap that would allow light through. This was determined by microscopy to correspond to a gap of 5 μm.

Liquid samples were taken for rheometry during processing. A TA Instruments AR 2000 EX rheometer measured viscosity of a sample between a flat plate accessory and a Peltier plate maintained at 25 °C. For DC electrical conductivity, samples were sanded into a rectangular shape, two opposing ends painted with silver paint, and resistance measured by a standard multimeter. For high resistance values, electrical impedance spectroscopy at 5 V over a frequency range of 0.1 Hz to 1 MHz using a Gamry Potentiostat 3000. Scanning electron microscopy (SEM) was performed with a Zeiss Supra 50VP SEM on samples that had been sputter coated with a 7−9 nm platinum layer prior to imaging. Transmission electron microscopy (TEM) was performed by a FEI-Tecnai T12 operated at 120 kV. Samples were prepared by microtoming sections at 100 nm nominal thickness and placing them on a 300 × 300 copper grid. Samples for mechanical testing were cast in dogbone shape molds and tested in the tensile orientation for modulus and yield strength. Five samples for each concentration were tested. X-ray diffraction was performed on a polished side of a cured composite sample on a Rigaku Smartlab diffractometer with a Cu anode X-ray tube at 30 mA/40 kV current using Bragg−Brentano geometry.

AUTHOR INFORMATION

Corresponding Author

*G. Palmese. E-mail: grp27@drexel.edu.

Notes

The authors declare no competing financial interest.

ACKNOWLEDGMENTS

The authors thank the Army Research Lab (Grant #W911NF-06-2-0013) for funding, Air Products for donating PACM curing agent, Arianna Watters for electrical impedance measurements and TEM imaging assistance, and Ed Basgall and Dmitri Barbosh of the Drexel Core Facilities, for help with SEM imaging and X-ray diffraction methodologies.

REFERENCES

(1) Singh, V.; Joung, D.; Zhai, L.; Das, S.; Khondaker, S. I.; Seal, S. Graphene based Materials: Past, Present and Future. *Prog. Mater. Sci.* **2011**, *56* (8), 1178−1271.

(2) Potts, J. R.; Dreyer, D. R.; Bielawski, C. W.; Ruoff, R. S. Graphene-based Polymer Nanocomposites. *Polymer* **2011**, *52* (1), 5−25.

(3) Koratkar, N. A. *Graphene in Composite Materials: Synthesis, Characterization, and Applications*; DEStech Publications: Lancaster, PA, 2013; p 1888.

(4) Sengupta, R.; Bhattacharya, M.; Bandyopadhyay, S.; Bhowmick, A. K. A Review on the Mechanical and Electrical Properties of Graphite and Modified Graphite Reinforced Polymer Composites. *Prog. Polym. Sci.* **2011**, *36* (5), 638−670.

(5) Park, S.; Ruoff, R. S. Chemical Methods for the Production of Graphenes. *Nat. Nano* **2009**, *4* (4), 217−224.

(6) Kuila, T.; Bose, S.; Mishra, A. K.; Khanra, P.; Kim, N. H.; Lee, J. H. Chemical Functionalization of Graphene and Its Applications. *Prog. Mater. Sci.* **2012**, *57* (7), 1061−1105.

(7) Salavagione, H. J.; Martínez, G.; Ellis, G. Recent Advances in the Covalent Modification of Graphene with Polymers. *Macromol. Rapid Commun.* **2011**, *32* (22), 1771−1789.

(8) Compton, O. C.; Nguyen, S. T. Graphene Oxide, Highly Reduced Graphene Oxide, and Graphene: Versatile Building Blocks For Carbon-based Materials. *Small* **2010**, *6* (6), 711−723.

(9) Kudin, K. N.; Ozbas, B.; Schniepp, H. C.; Prud'homme, R. K.; Aksay, I. A.; Car, R. Raman Spectra of Graphite Oxide and Functionalized Graphene Sheets. *Nano Lett.* **2007**, *8* (1), 36−41.

(10) Hernandez, Y.; Nicolosi, V.; Lotya, M.; Blighe, F. M.; Sun, Z.; De, S.; Mcgovern, I. T.; Holland, B.; Byrne, M.; Gun'Ko, Y. K.; Boland, J. J.; Niraj, P.; Duesberg, G.; Krishnamurthy, S.; Goodhue, R.; Hutchison, J.; Scardaci, V.; Ferrari, A. C.; Coleman, J. N. High-Yield Production of Graphene by Liquid-Phase Exfoliation Of Graphite. *Nat. Nano* **2008**, *3* (9), 563−568.

(11) Coleman, J. N. Liquid Exfoliation of Defect-Free Graphene. *Acc. Chem. Res.* **2012**, *46* (1), 14−22.

(12) Parviz, D.; Das, S.; Ahmed, H. S. T.; Irin, F.; Bhattacharia, S.; Green, M. J. Dispersions of Non-covalently Functionalized Graphene with Minimal Stabilizer. *ACS Nano* **2012**, *6* (10), 8857−8867.

(13) Georgakilas, V.; Otyepka, M.; Bourlinos, A. B.; Chandra, V.; Kim, N.; Kemp, K. C.; Hobza, P.; Zboril, R.; Kim, K. S. Functionalization of Graphene: Covalent and Non-covalent Approaches, Derivatives and Applications. *Chem. Rev.* **2012**, *112* (11), 6156−6214.

(14) Plechkova, N. V.; Seddon, K. R. Applications of Ionic Liquids in the Chemical Industry. *Chem. Soc. Rev.* **2008**, *37* (1), 123−150.

(15) Katsyuba, S. A.; Zvereva, E. E.; Vidiš, A.; Dyson, P. J. Application of Density Functional Theory and Vibrational Spectroscopy toward the Rational Design of Ionic Liquids. *J. Phys. Chem. A* **2006**, *111* (2), 352−370.

(16) Liu, N.; Luo, F.; Wu, H.; Liu, Y.; Zhang, C.; Chen, J. One-Step Ionic-Liquid-Assisted Electrochemical Synthesis of Ionic-Liquid-Functionalized Graphene Sheets Directly from Graphite. *Adv. Funct. Mater.* **2008**, *18* (10), 1518−1525.

(17) Lu, J.; Yang, J.-X.; Wang, J.; Lim, A.; Wang, S.; Loh, K. P. One-Pot Synthesis of Fluorescent Carbon Nanoribbons, Nanoparticles, and Graphene by the Exfoliation of Graphite in Ionic Liquids. *ACS Nano* **2009**, *3* (8), 2367−2375.

(18) Wang, X.; Fulvio, P. F.; Baker, G. A.; Veith, G. M.; Unocic, R. R.; Mahurin, S. M.; Chi, M.; Dai, S. Direct Exfoliation of Natural Graphite into Micrometre Size Few Layers Graphene Sheets Using Ionic Liquids. *Chem. Commun.* **2010**, *46* (25), 4487−4489.

(19) Kislenko, S. A.; Samoylov, I. S.; Amirov, R. H. Molecular Dynamics Simulation of the Electrochemical Interface between a Graphite Surface and the Ionic Liquid [BMIM][PF6]. *Phys. Chem. Chem. Phys.* **2009**, *11* (27), 5584−5590.

(20) Wang, J.; Chu, H.; Li, Y. Why Single-Walled Carbon Nanotubes Can Be Dispersed in Imidazolium-based Ionic Liquids. *ACS Nano* **2008**, *2* (12), 2540−2546.

(21) Rahmathullah, M. A. M.; Jeyarajasingam, A.; Merritt, B.; Vanlandingham, B.; Mcknight, S. H.; And Palmese, G. R. Room Temperature Ionic Liquids as Thermally Latent Initiators for Polymerization of Epoxy Resins. *Macromolecules* **2009**, *42* (9), 3219−3221.

(22) Throckmorton, J. A.; Watters, A. L.; Geng, X.; Palmese, G. R. Room Temperature Ionic Liquids for Epoxy Nanocomposite Synthesis: Direct Dispersion and Cure. *Compos. Sci. Technol.* **2013**, *86* (0), 38−44.

(23) Watters, A. L.; Palmese, G. R. Ultralow Percolation Threshold Of Single Walled Carbon Nanotube-Epoxy Composites Synthesized via an Ionic Liquid Dispersant/Initiator. *Mater. Res. Express* **2014**, *1* (3), 035013.

DOI: 10.1021/acsami.5b03465
ACS Appl. Mater. Interfaces 2015, 7, 14870−14877

(24) Watters, A.; Cuadra, J.; Kontsos, A.; Palmese, G. Processing-Structure−Property Relationships of SWNT−Epoxy Composites Prepared Using Ionic Liquids. *Composites, Part A* **2015**, *73* (0), 269−276.
(25) Bang, J. H.; Suslick, K. S. Applications of Ultrasound to the Synthesis of Nanostructured Materials. *Adv. Mater.* **2010**, *22* (10), 1039−1059.
(26) Suslick, K. S. Sonochemistry. *Science* **1990**, *247*, 1439−1445.
(27) Xia, Z. Y.; Pezzini, S.; Treossi, E.; Giambastiani, G.; Corticelli, F.; Morandi, V.; Zanelli, A.; Bellani, V.; Palermo, V. The Exfoliation of Graphene in Liquids by Electrochemical, Chemical, and Sonication-Assisted Techniques: A Nanoscale Study. *Adv. Funct. Mater.* **2013**, *23* (37), 4684−4693.
(28) Łoś, S.; Duclaux, L.; Alvarez, L.; Hawełek, Ł.; Duber, S.; Kempiński, W. Cleavage and Size Reduction of Graphite Crystal Using Ultrasound Radiation. *Carbon* **2013**, *55* (0), 53−61.
(29) Bracamonte, M. V.; Lacconi, G. I.; Urreta, S. E.; Foa Torres, L. E. F. On the Nature of Defects in Liquid-Phase Exfoliated Graphene. *J. Phys. Chem. C* **2014**, *118* (28), 15455−15459.
(30) Guiáshang, N. Controllable Selective Exfoliation of High-Quality Graphene Nanosheets and Nanodots by Ionic Liquid Assisted Grinding. *Chem. Commun.* **2012**, *48* (13), 1877−1879.
(31) Wakabayashi, K.; Brunner, P. J.; Masuda, J. I.; Hewlett, S. A.; Torkelson, J. M. Polypropylene-Graphite Nanocomposites Made by Solid-State Shear Pulverization: Effects of Significantly Exfoliated, Unmodified Graphite Content on Physical, Mechanical and Electrical Properties. *Polymer* **2010**, *51* (23), 5525−5531.
(32) Leon, V.; Quintana, M.; Herrero, M. A.; Fierro, J. L. G.; Hoz, A. D. L.; Prato, M.; Vazquez, E. Few-Layer Graphenes from Ball-Milling of Graphite with Melamine. *Chem. Commun.* **2011**, *47* (39), 10936−10938.
(33) León, V.; Rodriguez, A. M.; Prieto, P.; Prato, M.; Vázquez, E. Exfoliation of Graphite with Triazine Derivatives under Ball-Milling Conditions: Preparation of Few-Layer Graphene via Selective Noncovalent Interactions. *ACS Nano* **2013**, *8* (1), 563−571.
(34) Paton, K. R.; Varrla, E.; Backes, C.; Smith, R. J.; Khan, U.; O'Neill, A.; Boland, C.; Lotya, M.; Istrate, O. M.; King, P.; Higgins, T.; Barwich, S.; May, P.; Puczkarski, P.; Ahmed, I.; Moebius, M.; Pettersson, H.; Long, E.; Coelho, J.; O'Brien, S. E.; Mcguire, E. K.; Sanchez, B. M.; Duesberg, G. S.; Mcevoy, N.; Pennycook, T. J.; Downing, C.; Crossley, A.; Nicolosi, V.; Coleman, J. N. Scalable Production of Large Quantities of Defect-Free Few-Layer Graphene by Shear Exfoliation in Liquids. *Nat. Mater.* **2014**, *13* (6), 624−630.
(35) Yi, M.; Shen, Z. Kitchen Blender for Producing High-Quality Few-Layer Graphene. *Carbon* **2014**, *78* (0), 622−626.
(36) Chen, J.; Duan, M.; Chen, G. Continuous Mechanical Exfoliation of Graphene Sheets via Three-Roll Mill. *J. Mater. Chem.* **2012**, *22* (37), 19625−19628.
(37) Yasmin, A.; Abot, J. L.; Daniel, I. M. Processing of Clay/Epoxy Nanocomposites by Shear Mixing. *Scr. Mater.* **2003**, *49* (1), 81−86.
(38) Yasmin, A.; Daniel, I. M. Mechanical and Thermal Properties of Graphite Platelet/Epoxy Composites. *Polymer* **2004**, *45* (24), 8211−8219.
(39) Yasmin, A.; Luo, J.-J.; Daniel, I. M. Processing of Expanded Graphite Reinforced Polymer Nanocomposites. *Compos. Sci. Technol.* **2006**, *66* (9), 1182−1189.
(40) Thostenson, E. T.; Ziaee, S.; Chou, T.-W. Processing and Electrical Properties of Carbon Nanotube/Vinyl Ester Nanocomposites. *Compos. Sci. Technol.* **2009**, *69* (6), 801−804.
(41) Thostenson, E. T.; Chou, T.-W. Processing-Structure-Multi-Functional Property Relationship in Carbon Nanotube/Epoxy Composites. *Carbon* **2006**, *44* (14), 3022−3029.
(42) Gojny, F. H.; Wichmann, M. H. G.; Köpke, U.; Fiedler, B.; Schulte, K. Carbon Nanotube-Reinforced Epoxy-Composites: Enhanced Stiffness and Fracture Toughness at Low Nanotube Content. *Compos. Sci. Technol.* **2004**, *64* (15), 2363−2371.
(43) Jogun, S.; Zukoski, C. F. Rheology of Dense Suspensions of Platelike Particles. *J. Rheol.* **1996**, *40* (6), 1211−1232.
(44) Li, J.; Kim, J.-K. Percolation Threshold of Conducting Polymer Composites Containing 3D Randomly Distributed Graphite Nanoplatelets. *Compos. Sci. Technol.* **2007**, *67* (10), 2114−2120.
(45) Zaman, I.; Phan, T. T.; Kuan, H.-C.; Meng, Q.; Bao La, L. T.; Luong, L.; Youssf, O.; Ma, J. Epoxy/Graphene Platelets Nanocomposites with Two Levels of Interface Strength. *Polymer* **2011**, *52* (7), 1603−1611.
(46) Soule, D. E.; Nezbeda, C. W. Direct Basal-Plane Shear in Single-Crystal Graphite. *J. Appl. Phys.* **1968**, *39* (11), 5122−5139.
(47) Liu, Z.; Zhang, S.-M.; Yang, J.-R.; Liu, J.; Yang, Y.-L.; Zheng, Q.-S. Interlayer Shear Strength of Single Crystalline Graphite. *Acta Mech. Sin.* **2012**, *28* (4), 978−982.
(48) Shen, Y. K.; Wu, H. A. Interlayer Shear Effect on Multilayer Graphene Subjected to Bending. *Appl. Phys. Lett.* **2008**, *100*, 101909.
(49) Popov, A. M.; Lebedeva, I. V.; Knizhnik, A. A.; Lozovik, Y. E.; Potapkin, B. V. Barriers to Motion and Rotation of Graphene Layers Based on Measurements of Shear Mode Frequencies. *Chem. Phys. Lett.* **2012**, *536*, 82−86.
(50) Savini, G.; Dappe, Y. J.; Öberg, S.; Charlier, J. C.; Katsnelson, M. I.; Fasolino, A. Bending Modes, Elastic Constants and Mechanical Stability of Graphitic Systems. *Carbon* **2011**, *49* (1), 62−69.

DOI: 10.1021/acsami.5b03465
ACS Appl. Mater. Interfaces 2015, 7, 14870−14877